

A likely flyby of binary protostar Z CMa caught in action

Ruobing Dong¹, Hanyu Baobab Liu², Nicolás Cuello³, Christophe Pinte⁴, Péter Ábrahám^{5,17}, Eduard Vorobyov^{6,16}, Jun Hashimoto⁷, Ágnes Kóspál^{5,13,17}, Eugene Chiang⁸, Michihiro Takami², Lei Chen⁵, Michael Dunham⁹, Misato Fukagawa¹⁰, Joel Green¹¹, Yasuhiro Hasegawa¹², Thomas Henning¹³, Yaroslav Pavlyuchenkov¹⁴, Tae-Soo Pyo¹⁵, Motohide Tamura^{7,10,18}

¹*Department of Physics & Astronomy, University of Victoria, Victoria, BC, V8P 1A1, Canada*

²*Institute of Astronomy and Astrophysics, Academia Sinica, Taipei 10617, Republic of China*

³*Univ. Grenoble Alpes, CNRS, IPAG, F-38000 Grenoble, France*

⁴*Monash Centre for Astrophysics (MoCA) and School of Physics and Astronomy, Monash University, Clayton VIC 3800, Australia*

⁵*Konkoly Observatory, Research Centre for Astronomy and Earth Sciences, Eötvös Loránd Research Network (ELKH), Konkoly-Thege Miklós út 15-17, 1121 Budapest, Hungary*

⁶*University of Vienna, Department of Astrophysics, Vienna, 1180, Austria*

⁷*Astrobiology Center, National Institutes of Natural Sciences, 2-21-1 Osawa, Mitaka, Tokyo 181-8588, Japan*

⁸*Department of Astronomy, University of California at Berkeley, Berkeley, CA 94720-3411, USA*

⁹*Department of Physics, State University of New York at Fredonia, Fredonia, NY 14063, USA*

¹⁰*National Astronomical Observatory of Japan, 2-21-1, Osawa, Mitaka, Tokyo, 181-8588, Japan*

¹¹*Space Telescope Science Institute (STScI), Baltimore, MD 21218, USA*

¹²*Jet Propulsion Laboratory, California Institute of Technology, Pasadena, CA 91109, USA*

¹³*Max-Planck-Institut für Astronomie, Heidelberg 69117, Germany*

¹⁴*Institute of Astronomy, Russian Academy of Sciences, Moscow, Russia*

¹⁵*Subaru Telescope, National Astronomical Observatory of Japan, National Institutes of Natural Sciences, HI 96720, USA*

¹⁶*Research Institute of Physics, Southern Federal University, Rostov-on-Don 344090, Russia*

¹⁷*ELTE Eötvös Loránd University, Institute of Physics, Pázmány Péter sétány 1/A, 1117 Budapest, Hungary*

¹⁸*Department of Astronomy, The University of Tokyo, Tokyo 113-0033, Japan*

Close encounters between young stellar objects in star forming clusters are expected to dramatically perturb circumstellar disks. Such events are witnessed in numerical simulations of star formation¹⁻³, but few direct observations of ongoing encounters have been made. Here we report sub-0".1 resolution Atacama Large Millimeter Array (ALMA) and Jansky Very Large Array (JVLA) observations towards the million year old binary protostar Z CMa in dust continuum and molecular line emission. A point source ~ 4700 au from the binary has been discovered at both millimeter and centimeter wavelengths. It is located along the extension of a ~ 2000 au streamer structure previously found in scattered light imaging, whose counterpart in dust and gas emission is also newly identified. Compar-

ison with simulations shows signposts of a rare flyby event in action. Z CMA is a “double burster”, as both binary components undergo accretion outbursts⁴, which may be facilitated by perturbations to the host disk by flybys^{5–8}.

Z Canis Majoris (hereafter Z CMA) is a pre-main sequence binary system located at ~ 1125 pc in the Canis Major R1 association (Methods). The southeast component belongs to a class of outbursting protostars called FUors, inferred based on the characteristic broad doubled optical absorption lines⁹. The $0''.1$ apart northwest component has displayed repeated outbursts in the past few decades, resembling the EXor type outbursting protostars¹⁰. The pair has been spatially resolved in adaptive optics observations at multiple epochs^{10,11}, and their motion is consistent with a face-on circular orbit composed of a $5M_{\odot}$ (EXor component) and $1M_{\odot}$ star (FUor component)^{12,13}.

Previous spatially unresolved millimeter observations reported a total flux density of 26 ± 1 mJy at 1.4 mm and 2.1 ± 0.1 mJy at 7 mm¹⁴. We observed the Z CMA system in continuum and molecular line emission at around 224 GHz (1.3 mm) using the Atacama Large Millimeter Array (ALMA; Methods), and in continuum emission at 33 GHz (9 mm) using the Jansky Very Large Array (JVLA; Methods). Fig. 1 shows the synthesized 1.3 and 9 mm continuum emission images. In total we detect four point like sources (A–D) at 1.3 mm. Two of them, A and B, are the central binary. Gaussian fitting of the flux indicates that both are surrounded by disks ~ 20 au in size, potentially containing mm-sized dust particles. This is in line with millimeter observations of outbursting protostars in general^{15,16}, which often show compact dust emission. At 9 mm, both sources are detected too, as well as a jet-like structure $0''.1$ in length likely originated from B. Gas observations show prominent outflow and cavity structures on large scales (Extended Data Figs. 1 and 2).

The other two 1.3 mm sources, C and D, were previously unknown. In the continuum map imaged with Robust = 0, C is detected with a flux density of 700 ± 40 mJy and a signal-to-noise ratio (SNR) of 27 at $4''.2$ (4725 au), while D is detected with a flux density of 550 ± 24 mJy and a SNR of 21 at $0''.8$ (900 au; Methods; Extended Data Table 1). They have spectral line counterparts, as shown in Fig. 2 (most noticeable in $C^{18}O$ and SO emission; Methods), that appear to connect to the circumbinary environment of Z CMA. We conclude that both are likely physically associated with the system rather than being foreground or background sources. In addition, component C is detected at 9 mm by JVLA with SNR=5 (Methods). Gaussian fitting of its flux indicates that C is marginally resolved at both 1.3 and 9 mm with a deconvolved size of 40–50 au. Its spectral index α between the two wavelengths is 1.6 ± 0.1 . This low index may be explained by non-thermal contributions at 9 mm, a hot central source embedded in an optically thick medium¹⁷, or strongly scattering dust at mm wavelengths¹⁸. Component D cannot be recovered in the JVLA observations. It may be a fragment that has recently formed from turbulent fragmentation in the disk or surrounding cloud^{19,20}, in which scenario it is only visible at mm but not cm wavelength due to its youth and associated insufficient dust growth. Further characterizations of these sources are presented in the Methods section and Supplementary Information, including the intensity weighted velocity (moment 1) maps. No other point sources have been detected in 1.3 mm continuum emission imaged with Robust = 0 with a $3\text{-}\sigma$ detection limit of $78 \mu\text{Jy}$, equivalent to a dust mass of $3 M_{\oplus}$ (Methods).

Near-infrared imaging observations have revealed a large disk in scattered light extending to ~ 1500 au²¹. Remarkably, the disk has a $\sim 2''$ long filamentary structure in the southwest, discovered in Keck adaptive optics observations¹² and confirmed by VLT and Subaru in polarized light imaging^{13,21} (Fig. 1). In our observations the inner $\sim 1''$ of this streamer is detected in 1.3 mm continuum, with a total flux density of 3 ± 0.6 mJy and an estimated solid mass of $119 \pm 24 M_{\oplus}$ (Methods). It is detected in ^{13}CO and C^{18}O emission as well (Fig. 3). The detection in dust and gas emission suggests that the streamer is a dust surface density enhancement.

The origin of the streamer has been a long-standing puzzle. It has been variously hypothesized to be the wall of a cavity created by a molecular outflow¹³, a spiral arm produced by gravitational instability^{21,22}, or the relic of a recently captured low mass ($\sim 0.01 M_{\odot}$) cloudlet⁷. The newly discovered source C at the end of the streamer points to another possible scenario that we consider the most likely: C may be a young stellar object (YSO) that has recently performed a flyby around Z CMa, and the streamer is a structure produced by this tidal interaction event.

Tidal interactions between a protoplanetary disk and a flyby intruder are known to strongly perturb the disk²³. Depending on the angle β between the angular momentum vector of the disk and that of the intruder (with respect to the host), flyby events can be categorized as prograde ($\beta < 90^\circ$) or retrograde ($90^\circ < \beta \leq 180^\circ$). Prograde flybys typically induce a pair of spiral arms in the disk on global scale, with the primary arm pointing towards the intruder and the secondary arm roughly 180° away in the azimuth. These arms are due to the combined effect of the intruder’s gravitational perturbation and the displacement of the centre of mass of the system²³. They are most prominent and symmetric when $\beta = 0^\circ$ (coplanar and prograde flyby), and their strength and symmetry decrease as β increases. Retrograde flybys have much weaker effects on the disk, unless it is deeply penetrating⁶. In non-coplanar flybys, the primary arm can be lifted above the disk plane to keep pointing to the intruder, while the secondary arm is embedded in the disk⁶.

Fig. 4 shows a simulated flyby event (Methods; Extended Data Fig. 3), in which an intruder flies by a single disk-hosting primary with an intruder/primary mass ratio $q = 0.3$. We do not expect the binary nature of Z CMa to significantly affect the outcome of the flyby at distances more than 10 times the binary separation. The intruder approaches the host on a prograde parabolic orbit inclined with respect to the host’s disk by $\beta = 45^\circ$. The pericenter is at $R_{\text{peri}} = 3000$ au and in the disk plane. The size of the initial disk surrounding the host is $R_{\text{out}} = 840$ au, thus the flyby is non-penetrating. A pair of spiral arms are produced in the density space with comparable strengths. The two arms, however, have different illuminations, because they are in different planes. The primary arm pointing to the flyby is in the orbital plane of the flyby, and the light path from the host star is unobscured (the host star is assumed to be much more luminous than the intruder at near-infrared wavelengths). The arm is expected to be present in dust and gas emission due to its enhanced density²⁴. In contrast, the secondary arm is in the plane of the circumprimary disk and is much less well illuminated by the host star²⁴. The overall morphology of the model, with one prominent arm extending beyond the main disk and pointing towards the intruder, resembles the observations of the Z CMa system (Fig. 4). We note that the model does not represent a unique solution; instead it is one representative

example that produces an overall match to the observations (Methods).

Component C has not been identified at optical and infrared wavelengths in the SDSS, Gaia, 2MASS, and WISE databases. Analysis of archival Keck adaptive optics imaging observations of Z CMa yields an upper limit of 21.9 mag for C in H -band apparent magnitude (Methods; Extended Data Fig. 4), corresponding to the photosphere of a Myr-old planetary mass object at 1125 pc, or a solar mass YSO experiencing ~ 10 mag of extinction²⁶. Past simulations and our tests indicate that an intruder with $q \lesssim 0.1$ has difficulties in exciting the observed streamer, putting a lower limit of $\sim 0.6 M_{\odot}$ in mass for C (Methods). Therefore, C is likely heavily extinguished. A flyby intruder may capture material from the host disk to form an envelope or a disk, depending on the angle and the level of penetration of the flyby^{6,24,27}. The intruder may also possess a natal disk prior to the flyby. The detection of C in both dust and gas emission indicates its possession of circumstellar material, which may originate from either scenario (Methods). A heavy extinction may be caused by, for example, an edge on circumstellar disk. Adopting conventional assumptions, its 1.3 mm flux density translates to $\sim 28 M_{\oplus}$ of solids in the circumstellar environment. Future observations at mid- to far-infrared wavelengths are needed to probe the spectral energy distribution of C to further constrain its properties.

Simulations have shown that a prograde flyby may exert gravitational torques and lead to shocks and angular momentum redistribution in the disk, and drive material to smaller radii around the binary^{5,23,28–30}. This may trigger accretion outbursts with the accretion rate jumping up by one order of magnitude shortly after pericenter passage⁶. This appears consistent with the double burster nature of Z CMa. Isolated protostars with masses from $0.1 - 40 M_{\odot}$ spend on average $1 - 10\%$ of the time in self-induced outbursts^{31,32}. Thus, the chance of witnessing a binary in this mass range undergoing accretion outbursts simultaneously is expected to be $\lesssim 1\%$ if the two outbursts are independent of each other. Given the small number of protostar binaries that have been monitored with sufficient depth and temporal coverage to enable detections of outbursts, the double burster nature of Z CMa implies that whatever has triggered the outbursts in one may have triggered those in the other. This is plausible if both are facilitated by the flyby.

While our multi-wavelength observations of the Z CMa system lend support for a possible recent flyby event, alternative scenarios accounting for the observations exist. For example, it is possible that C is a self-gravitating clump previously formed in the dense environment at smaller radii that has subsequently been ejected due to dynamical interactions with the stars and/or other clumps³³. Such clumps may form by fragmentation of gravitationally unstable disks^{34,35}. In such an event, the ejecta drives a bow shock, which may appear to be filamentary streamers in observations²⁷. The binary nature of Z CMa, which promotes dynamical scattering, encourages this scenario. However, the bow shock behind the ejecta typically has two edges with roughly equal strengths (and both of them are expected to be within the disk plane). In addition, the resulting streamers are more prominent closer to the ejecta²⁷, instead of the other way around as observed. We thus conclude that the ejecta scenario is less likely. Recent observations have shown multiple filamentary structures as infall and accretion streamers connecting a cloud to the disk in a few systems^{36–40}. However unlike in those cases, Z CMa’s streamer is not known to be connected to a large-scale cloud, and no other tails similar in strength and size have been found. Three-dimensional gravo-magnetohydrodynamic

simulations have also shown that streamers and clumps can form in turbulent fragmentation in filamentary giant molecular clouds^{19,20}. While it is possible that the observed streamer and source C form in this manner, the fact that the streamer points toward the source C shows that the flyby scenario is compelling.

Our discovery of C at a special location with respect to the streamer, the unique morphology of the disk in multi-wavelength imaging observations, and the double burster nature of Z CMa show signposts of a flyby in action around a binary young stellar object. These set the Z CMa system apart from a handful of other flyby candidate systems (Methods). Flybys during star formation are expected to dramatically affect the disk and the planet formation processes within it. For example, the extremely long period object Sedna⁴¹ has prompted the hypothesis that the solar system may have experienced close encounters with intruders in its infancy⁴². Future high spatial resolution observations at both mm and NIR wavelengths may find more systems like Z CMa by identifying an intruder and its dynamically induced structures, thus establishing an empirical estimate of the frequency of flybys and better assessing its role in the evolution of protoplanetary disks. In particular, it would be exciting to search for flyby events in outbursting protostar systems, to test the hypothesis that flyby may trigger accretion outbursts. Such studies will also shed light on the formation and evolution of binary and multiple systems⁴³.

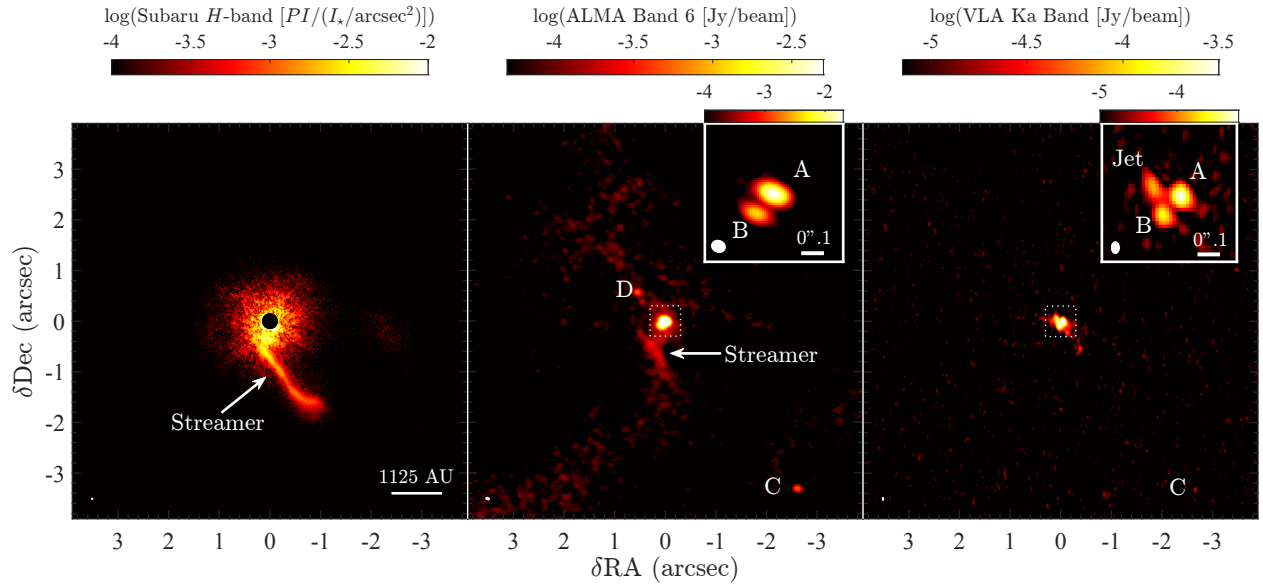


Figure 1: **Observations of the Z CMa system.** The center is at component A (ALMA coordinates RA, Dec = $07^{\text{h}}03^{\text{m}}43^{\text{s}}.154$, $-11^{\circ}33'06''.13$). Left: Subaru *H*-band scattered light image with an angular resolution of 0.07 arcsec^{21} . Middle: ALMA 1.3 mm dust continuum emission with Briggs robust = 2 (beam size $115 \times 95 \text{ mas}$, P.A. = 74°). The inset is a zoom in of the inner $0.6 \times 0.6 \text{ arcsec}$ region (dotted box) with Briggs Robust = -2 (beam size $71 \times 42 \text{ mas}$, P.A. = 68°). Right: JVLA 9 mm dust continuum emission with Briggs Robust = 2 (beam size $100 \times 66 \text{ mas}$, P.A. = 4°). The inset is a zoom in of the inner $0.6 \times 0.6 \text{ arcsec}$ region (dotted box) with Briggs Robust = -2 (beam size $62 \times 45 \text{ mas}$, P.A. = 1°). In all panels, the angular resolution or the beam is marked at the lower left corner. The four point sources detected in the ALMA observations, and the counterparts of A, B, and C and a jet detected in the JVLA observations, are labeled.

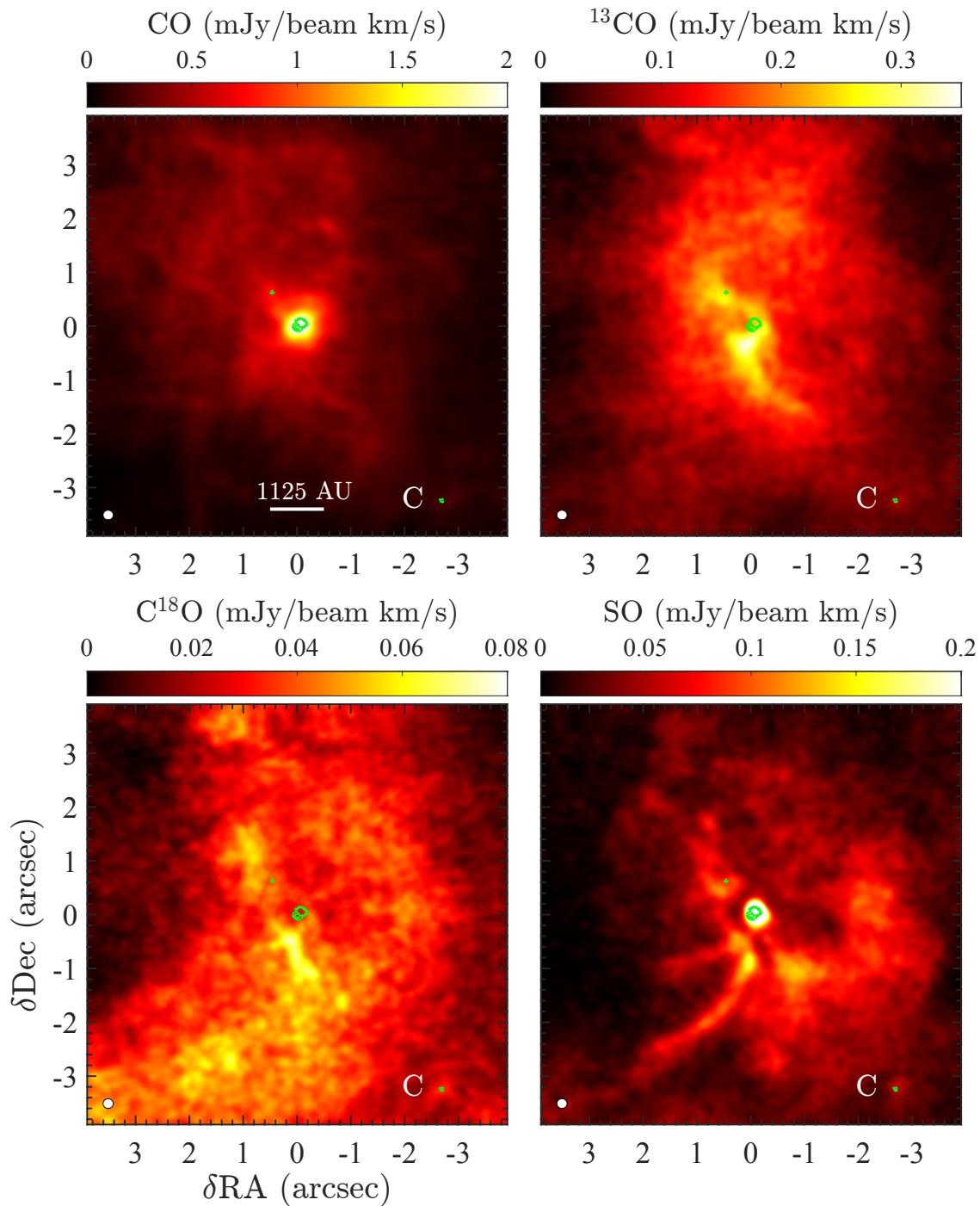


Figure 2: **Integrated intensity (moment 0) maps of the ^{12}CO (2-1), ^{13}CO (2-1), C^{18}O (2-1), and $\text{SO } ^3\Sigma 6(5)\text{-}5(4)$ transitions.** The beam size ($0.19'' \times 0.18''$; P.A.= 88°) is marked at the lower left corner. The Robust = 0 weighted 224 GHz continuum image (beam size $0''.075 \times 0''.047$; P.A.= 65°) is shown in green contours at 0.13 and 1.3 mJy beam^{-1} levels (5 and $50 \times$ the root mean square noises) to highlight the four compact continuum sources. The ALMA/JVLA source C is labeled.

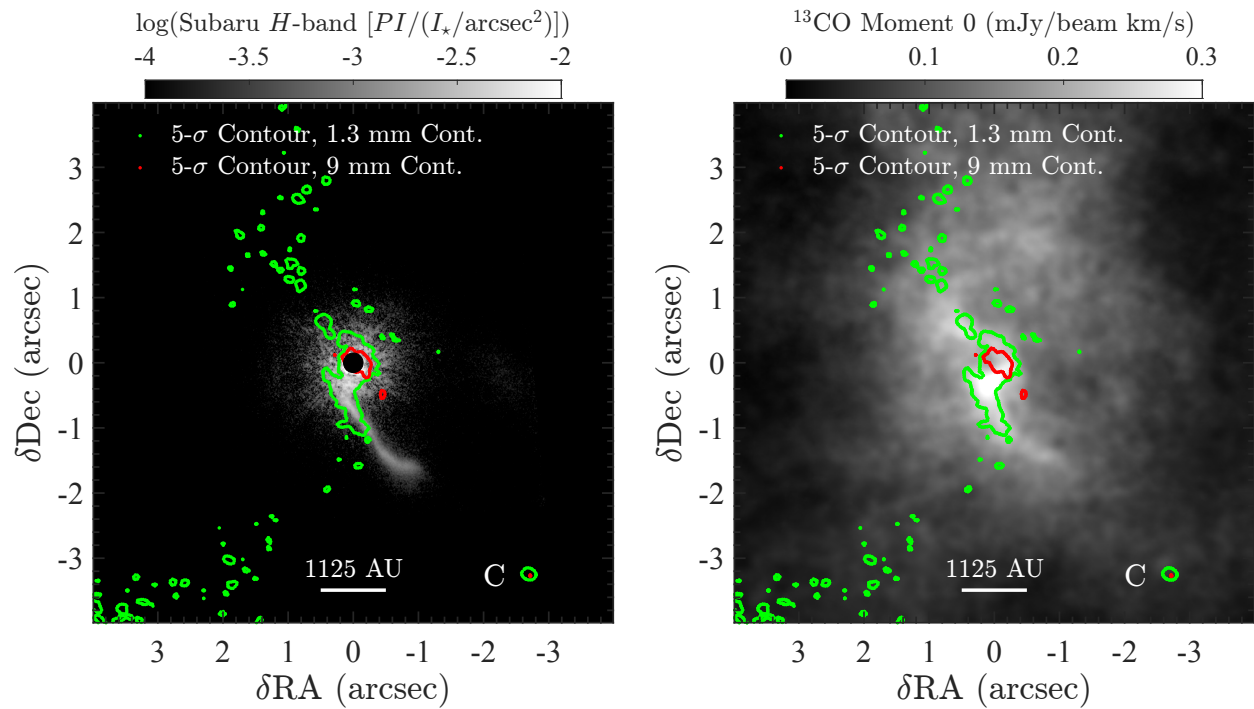


Figure 3: **Subaru H -band image (left) and ^{13}CO moment 0 map (right) overlaid with the 5- σ contours in ALMA 1.3 mm continuum emission (green) and in JVLA 9 mm continuum emission (red).** Both the ALMA and JVLA maps are imaged with Robust = 2. The ALMA/JVLA source C is labeled.

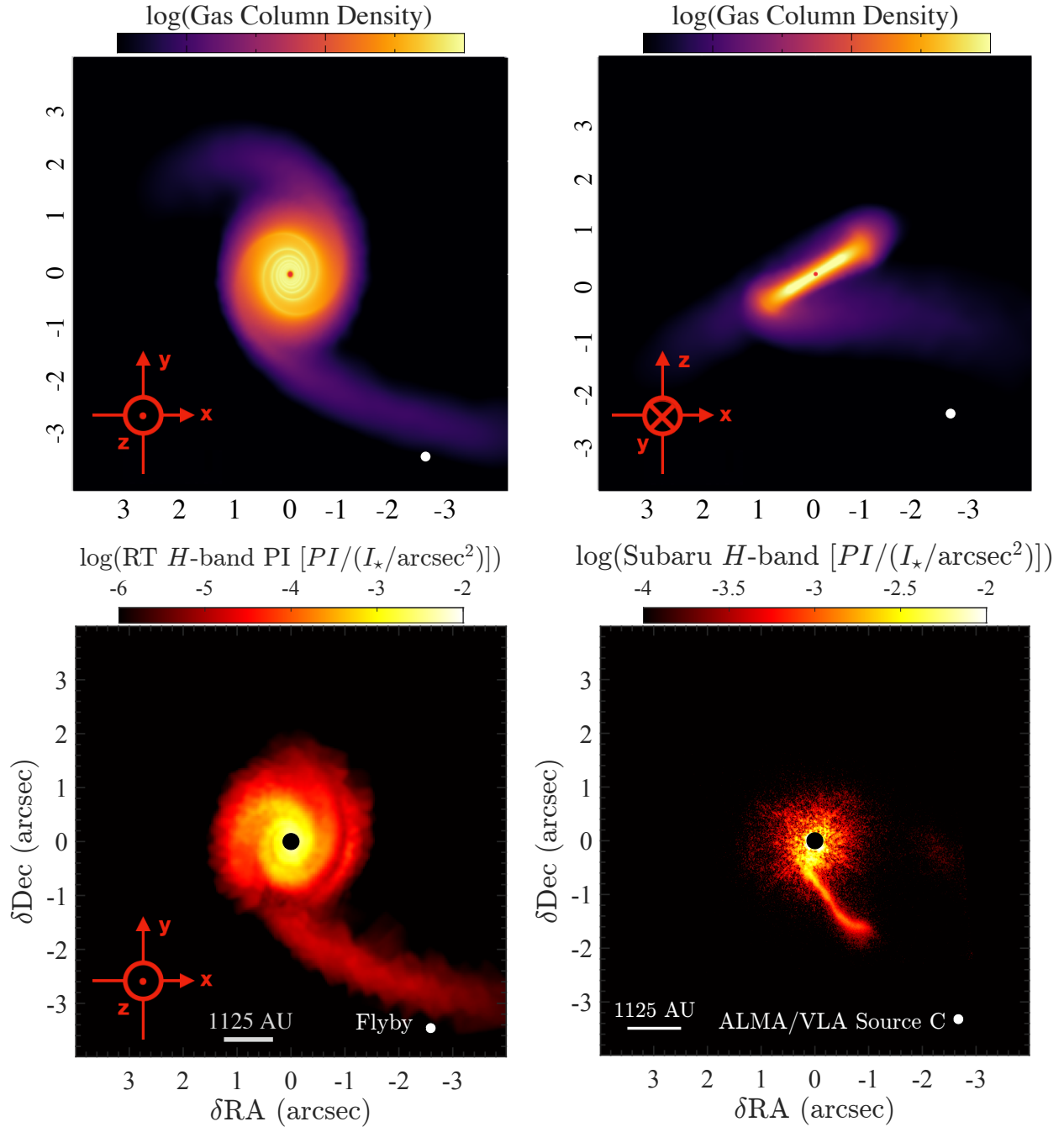


Figure 4: **Comparing simulations with observations.** (Top row) Two views of the gas column density in the hydrodynamical simulation of a stellar flyby. The system is shown 14 kyr after the perturber has gone through pericentre. The resulting H -band synthetic image in polarized light obtained through radiative transfer simulation (bottom left) is to be compared with the Subaru H -band polarized light observation (bottom right). In the synthetic image the line of sight is in the z direction.

Methods

Distance of Z CMa. The distance to Z CMa is controversial. The Gaia Early Data Release 3 (EDR3) measured a parallax of 2.035 ± 0.632 mas⁴⁴, corresponding to a distance of 491_{-116}^{+221} pc. However, the Renormalised Unit Weight Error (ruwe) parameter is 36.798, a value far exceeding the generally accepted upper limit of 1.4. It is a strong implication for unreliable parallax solution⁴⁴, possibly caused by the photometric variabilities of this system, or by the imperfect modeling of a disk bearing binary system as a single star.

In order to clarify the distance of Z CMa, we performed a Gaia EDR3-based analysis of Canis Major R1, the cluster in which Z CMa is considered to be a member^{45–47}. We compiled a list of 62 young stars in CMa R1, all with $\text{ruwe} \leq 1.4$, from the literature^{48–50}. The distribution of their distances exhibits a strong single peak at 1125 ± 30 pc, with only one star located closer than 650 pc. The area occupied by CMa R1 members on the sky coincides well with the position of Z CMa. The selected cluster members have a tight distribution in proper motion: $\text{pm}_{RA} = -4.49 \pm 0.2$ mas yr⁻¹, $\text{pm}_{DE} = +1.59 \pm 0.19$ mas yr⁻¹. The proper motion of Z CMa, taken either from Gaia EDR3 or from Ducourant et al.⁵¹, matches that of CMa R1 within 3σ in right ascension, and is higher by not more than 2.25 mas yr⁻¹ in declination. We conclude that Z CMa fits in the CMa R1 cluster in both coordinates and proper motion, and that there is no hint for additional star formation activity in the foreground of the cluster. Thus, we assume that Z CMa is a member of Canis Major R1, and adopt a distance of 1125 pc.

ALMA observations. We performed the ALMA (Project 2016.1.00110.S) observations on 2016 October 21 in the C40-6 array configuration. The minimum and maximum baseline lengths were 15 and 1800 meters. The gain calibrator was J0730-1141, and the absolute flux and passband calibrator was J0705+1231. We adopted the 0.86 Jy absolute flux and the -0.64 spectral index for J0705+1231 at the representative frequency 223.165 GHz, which were derived from interpolating the grid survey of ALMA. The bootstrapped flux of J0730-1141 was 1.1 Jy at 223.091 GHz. There were six spectral windows, of which the (central frequency, total bandwidth, and frequency channel width) are (230.585 GHz, 234 MHz, 61 kHz), (231.695 GHz, 1875 MHz, 976 kHz), (220.394 GHz, 117 MHz, 61 kHz), (219.556 GHz, 59 MHz, 61 kHz), (219.945 GHz, 59 MHz, 61 kHz), (216.812 GHz, 1875 MHz, 488 kHz), respectively.

We performed the ALMA long baseline (C40-8) configuration observations on 2017 September 07 (Project 2016.1.00110.S). The minimum and maximum baseline lengths are 168 and 6800 meters. The gain calibrator was J0654-1053, and the absolute flux and passband calibrator was J0705+1231. We adopted the 0.84 Jy absolute flux and the -0.67 spectral index for J0705+1231 at the representative frequency 223.162 GHz. The bootstrapped flux of J0654-1053 was 0.12 Jy at 223.088 GHz. The spectral setups were similar to that of the observations on 2016 October 21, except that the spectral windows at 231.695 GHz and 216.812 GHz were compromised to have 7812 kHz and 976 kHz frequency channel widths to suppress the data rate.

We performed the Atacama Compact Array (ACA) observations on 2017 July 09 (Project 2016.2.00168.S).

The gain, passband, and absolute flux calibrators were J0730-1141, J0522-3627, and J0854+2006, respectively. We adopted the 4.4 Jy absolute flux and the -0.46 spectral index for J0854+2006 at the representative frequency 223.144 GHz. The bootstrapped flux of J0730-1141 was 1.5 Jy at 223.071 GHz. The spectral setups were similar to that of the observations on 2016 October 21, except that the spectral window at 231.671 GHz has a smaller frequency channel width of 488 kHz.

We manually calibrated the data using the CASA v5.1.1 software package⁵². The gain calibrator for our ALMA long baseline observations in 2017 was faint. To yield reasonably high signal-to-noise (S/N) ratios when deriving the gain phase solutions, we first solved the phase offsets among spectral windows using the passband calibration scan. After applying the phase offsets solution, we then derived the gain phase solution by combining all spectral windows. The calibration of the ACA observations and the ALMA 12-m array observations in 2016 followed the standard procedure of ALMA quality assurance (i.e., QA2). After calibration, we fitted the continuum baseline and subtracted it from the spectral line data, using the CASA task `uvcontsub`. We jointly phase self-calibrated all observations based on the continuum data, and then applied the phase self-calibration solutions to both the continuum and the spectral line data.

The phase self-calibrated ALMA 12-m array and ACA data were jointly imaged. The Multi-Frequency Synthesis (MFS) imaging of the continuum data were performed using `CASA-clean`. To achieve a high intensity dynamic range, we imaged the upper sideband and lower sideband data separately using only one Taylor term. We then smoothed the upper sideband continuum image to the same angular resolution as the lower sideband continuum image, and then linearly combined them. The root-mean-square (RMS) noise level were estimated from the difference of the lower sideband and the smoothed upper sideband continuum images, which are 18, 26, and 34 $\mu\text{Jy beam}^{-1}$ in the case of Briggs Robust = 2, 0, -2 weighting, respectively. The corresponding synthesized beam sizes with these weightings are $\theta_{\text{maj}} \times \theta_{\text{min}}=0''.11 \times 0''.095$ (P.A.= 75°), $\theta_{\text{maj}} \times \theta_{\text{min}}=0''.078 \times 0''.046$ (P.A.= 66°), and $\theta_{\text{maj}} \times \theta_{\text{min}}=0''.071 \times 0''.042$ (P.A.= 68°).

Spectral line imaging were performed using the Miriad software package⁵³. We first imaged the ACA data alone. After correcting for the ACA primary beam attenuation, we multiplied the ACA images with the primary beam of the ALMA 12m dishes using `Miriad-demos`. We then re-generated the 12m primary beam attenuated ACA visibilities using `Miriad-uvmodel`. Finally, we jointly imaged the re-generated ACA visibility and the ALMA visibilities using `Miriad-invert`, `clean`, and `restor`, and corrected for the ALMA 12m dish primary beam attenuation after then. We compared the images of a few channels of ^{13}CO 2-1 produced this way, with those created with `CASA-clean` and `CASA-tclean` using mosaic mode, either applying `multi-scale clean` or not, and with and without imaging interactively (i.e., box cleaning). We found that the quality of the images created with our Miriad imaging strategy is not distinguishable from the best we can achieve with `CASA-clean` or `CASA-tclean`. In fact, without performing interactive imaging, we achieved a better image quality with our Miriad imaging strategy than with CASA. Jointly (mosaic) imaging ACA and ALMA data in CASA is extremely time consuming, such that interactively imaging the large number of spectral channels of our high spectral resolution observations is not practical for us. When imaging in CASA but without interactively boxing, the extended features (either real emission structures or sidelobe response) located in between the primary beams of the ACA and

the ALMA 12m dish often led to divergence of the `clean`, which by our experience is less predictable when the `multi-scale clean` is activated. When such features are presented, it is in fact also not trivial to decide how to place `clean` boxes, and that the imaging process became more subjective. Due to the high angular resolution of our observations, without activating `multi-scale clean`, the convergence of `CASA-clean` and `tclean` also became unrealistically slow for us. Therefore, we argue that our present spectral line imaging strategy is fair.

In continuum emission, we detect four compact sources. Two of them (A and B) compose the binary. The other two, C and D, are to the southwest and northeast of the binary, respectively. We performed 2D gaussian fitting using the task `imfit` in the image domain to measure their properties, and list them in Extended Data Table 1. Gas observations show prominent outflow and cavity structures on large scales, which dominate the signals in both the moment 0 (Extended Data Fig. 1) and moment 1 maps (Extended Data Fig. 2). ^{13}CO and C^{18}O do not trace the central binary very well, while the SO line does. All of these continuum sources have spectral line counterparts, so they are likely parts of the same system. The previously detected streamer in scattered light in the south of the binary has counterparts in both continuum and line emission.

JVLA observations. We performed JVLA Ka band (29-37 GHz) standard continuum mode observations toward ZCMA in the A array configurations on 2016 October 07 and 10 (project code: 16B-080). We took full RR, RL, LR, and LL correlator products. These observations had an overall duration of 6 hours, with ~ 2.7 hours of integration on the target source. The observations on October 07 and 10 covered the parallactic angle ranges of $333^\circ - 14^\circ$ and $343^\circ - 24^\circ$, respectively. After initial data flagging, 27 and 25 antennas were available for the respective of these two tracks of observations. The projected baseline lengths covered by these observations are in the range of $\sim 54-3579$ $k\lambda$, which yielded a $\theta_{\text{maj}} \times \theta_{\text{min}} = 0''.070 \times 0''.049$ (P.A. = 2.5°) synthesized beam (Briggs Robust = 0 weighting), and a maximum detectable angular scale of $\sim 1''.9$. We used the 3-bit sampler and configured the backend to have an 8 GHz simultaneous bandwidth coverage by 64 consecutive spectral windows, which were centered on 33 GHz sky frequency. The pointing and phase referencing centers for our target source is on R.A. = $07^{\text{h}}03^{\text{m}}43^{\text{s}}.164$ (J2000), decl. = $-11^\circ 33' 06''.200$ (J2000). Antenna pointing was calibrated approximately every hour. The complex gain calibrator J0730-1141 was observed for 40 s every 102 s to calibrate atmospheric and instrumental gain phase and amplitude fluctuation. We observed the bright quasar 3C147 for passband and absolute flux calibrations.

We manually followed the standard data calibration strategy using the CASA package, release 5.3.0. After implementing the antenna position corrections, weather information, gain-elevation curve, and opacity model, we bootstrapped delay fitting and passband calibrations, and then performed complex gain calibration. We applied the absolute flux reference to our complex gain solutions, and then applied all derived solution tables to the target source. We have performed gain phase self-calibration to remove the residual phase and delay errors.

We generated images using the CASA task `clean`. The image size is 6000 pixels in each dimension, and the pixel size is $0''.01$. To maximize sensitivity, we performed multi-frequency `clean` jointly for all observed spectral windows, which yielded a ~ 33 GHz averaged frequency and a Stokes I RMS noise level of $\sim 5.2 \mu\text{Jy beam}^{-1}$. The ALMA components A, B, and C are detected at 9 mm. We perform 2D gaussian fitting in the image domain using the CASA task `imfit` to measure their properties, and list them in the Extended Data Table 1. The ALMA source D was not detected.

Dust mass estimates. We adopt fluxes in continuum maps imaged with `Robust = 0` for dust mass estimates. Assuming that the circumstellar material is optically thin at 1.3 mm, we estimate its dust mass based on the integrated flux density as

$$M_{\text{dust}} = \frac{f_{\nu} d^2}{B_{\nu}(T_{\text{dust}}) \kappa_{\nu}}, \quad (1)$$

where d is the distance to the source, f_{ν} is the measured flux density, $B_{\nu}(T_{\text{dust}})$ is Planck function at the dust temperature T_{dust} , assumed to be 20 K, and κ_{ν} is the dust opacity κ , assumed to be $2.2 \text{ cm}^2 \text{ g}^{-1}$ at 224 GHz⁵⁴. The dust mass around C and D are estimated to be $28 \pm 1 M_{\oplus}$ and $22 \pm 1 M_{\oplus}$, respectively (the uncertainty only reflects the uncertainty in the flux measurement). For the streamer, given its measured total flux density in 1.3 mm continuum emission of $3 \pm 0.6 \text{ mJy}$, we estimate $M_{\text{dust}} = 119 \pm 24 M_{\oplus}$. As a reference, the $3\text{-}\sigma$ detection limit in our 1.3 mm continuum emission is $78 \mu\text{Jy}$, corresponding to a dust mass of $3 M_{\oplus}$. We note that the derived dust mass has large uncertainties due to the uncertainties in the dust temperature, opacity, and whether the emission is optically thin or thick.

Hydrodynamical and Radiative Transfer Simulations. We model the hydrodynamical evolution of the disk around Z CMA using the Smoothed Particle Hydrodynamics (SPH) PHANTOM code⁵⁵. The disk is modeled using 10^6 gas SPH particles and assuming a total disk mass of $0.3 M_{\odot}$ (thus a disk-to-star mass ratio of 5%). The initial disk surface density follows a power-law profile $\Sigma \propto R^{-1}$ and we assume that the disk is vertically isothermal. We adopt a mean Shakura–Sunyaev disk viscosity $\alpha_{\text{SS}} \approx 0.005$ by setting a fixed artificial viscosity parameter $\alpha_{\text{AV}} = 0.25$ and using the ‘disk viscosity’ flag of PHANTOM⁵⁶. The initial disk inner and outer radii are $R_{\text{in}} = 120 \text{ au}$ and $R_{\text{out}} = 840 \text{ au}$. R_{in} is not critical in this study since the main focus is on the arm morphology at large distances. The measured accretion rate onto the primary strongly depends on the choice of R_{in} and it is expected to increase during the encounter, especially for prograde inclined flybys⁶. During the tidal encounter, material in the disk is spread to $\sim 2500 \text{ au}$.

We model component C as the intruder. We consider D as a low mass clump that does not have a significant impact on the disk dynamics, thus ignored in the simulations. As mentioned in the main text, D may be a fragment that has recently formed from gravitoturbulent fragmentation in the disk or the surrounding cloud, in which scenario it is only visible at mm but not cm wavelength due to its youth and associated insufficient dust growth. For prograde flybys and companion-disk interaction in general⁵⁷, more prominent spiral arms form interior to the orbit of the perturber. The fact that D appears to be closer to the primaries than the streamer suggests that it is unlikely the driver of the streamer. Moreover, if D was a massive perturber deeply penetrating the disk, it would be expected to leave strong signatures in the disk, which is not observed in our multi-wavelength observations. In contrast, C is a much more robust candidate,

since it leaves the expected dynamical signatures in the disk.

We place the perturber on a parabolic prograde orbit at an angle of $\beta = 45^\circ$ with respect to the disk plane as shown in the sketch in Extended Data Fig. 3. The pericentre of the orbit is fixed along the line of nodes and at a distance of $r_{\text{peri}} = 3000$ au from the disk-hosting star. The perturber is initially placed at ten times R_{peri} . The masses of the host star and the perturber are set to $6 M_\odot$ and $1.8 M_\odot$, which give a mass ratio $q = 0.3$. Previous simulations^{6,23} have shown that as the mass ratio increases, the flyby event produces more prominent streamers, while the intruder rips off a larger fraction of the circumprimary disk, leaving a more compact disk afterward. The exact radial extent and morphology of the streamer depend on the mass ratio q , pericentre distance r_{peri} , initial disk size, and orbital inclination β . The mass of C is poorly constrained from the observations. Based on a limited number of tests we find that a minimum mass ratio of ~ 0.1 is needed in order to roughly reproduce the streamer with a companion at the current distance. We model both the star and the perturber as sink particles that interact with gas particles via gravity and accretion⁵⁸. Given the large spatial scales considered and for computational costs, we set the sink particle accretion radius to 10 au on both stars.

The flyby setup is publicly available in the PHANTOM repository. Here we consider a non-penetrating prograde flyby in order to trigger prominent spirals without capturing material around the perturber. The circumprimary disk is initially in the $x - y$ plane. In order to simultaneously match the appearance of the disk in scattered light and the orientation of C, we rotate the system by 105° , 30° , and 180° around the z -, y -, and x -axis (in clockwise sense and in that order). The line of sight is in the z direction (axis are shown in red in Fig. 4 and Extended Data Fig. 3).

We use the radiative transfer code MCFOST^{59,60} to generate synthetic polarized scattered light images. We build a Voronoi tessellation where each cell is associated to one SPH particle. The disk is passively heated by the two stellar sources: the host, and the intruder; however, the flyby star is turned off in simulating the scattered light image to mimic extinction by its circumstellar material (see below). We use isochrones^{61,62} at 3 Myr for the two sink particles of 6 and $1.8 M_\odot$, resulting in effective temperatures of 18400 and 4800 K and radii of 3.00 and $2.36 R_\odot$, respectively. We used 10^8 packets to compute the dust temperature structure and sample the specific intensity before generating the polarized scattered light images at $1.6 \mu\text{m}$ via a ray-tracing algorithm. The dust grain population is assumed to follow a power-law $dn(a) \propto a^{-3.5} da$ between 0.03 micron and 1 micron, and the total dust mass is set to 0.01 the gas mass from the SPH simulation. While grains are known to be able to grow to larger sizes in early stage disks⁶³, sub-micron-sized grains dominate the scattering of starlight. The presence of larger grains, not included in our simulations, is not expected to affect scattered light observations. The dust properties are calculated using the Mie theory assuming astrosilicate composition⁶⁴. The resulting synthetic observation in the H-band are shown in Fig. 4.

A prograde perturber may cause a strong gravitational pull able to excite the eccentricity of the material in the disk. This translates into enhanced stellar accretion and outbursts. The time delay between the pericenter passage and the peak of the accretion outbursts, as well as their duration, depend on a number of

parameters including the intruder-flyby mass ratio, the pericenter distance, the angle of the pericenter and the inclination of the intruder’s orbit relative to the circum-primary disk plane, and the size of the circum-primary disk. Cuello et al.⁶ carried out a sample of tests and found that for prograde flyby events the delay between the pericenter passage and the peak of the outbursts is on the order of 10% of the Keplerian orbital period at the pericenter, and the outbursts temporally coincide with prominent spiral arms in the disk (they both fade away with time). Meanwhile the outbursts can last for at least thousands of years. These are broadly consistent with our model. We caution that in current simulations⁶ the stellar accretion is modeled as material crossing the inner boundary of the disk at 10 AU. Future investigations are needed to model the disk dynamics in the inner disk to better quantify the accretion outburst timescales.

Our model demonstrates that a flyby event can produce one prominent arm extending beyond the outer edge of the circumprimary disk and pointing to the intruder. We note that the model is not designed to perfectly reproduce the observations, and no extensive parameter space survey has been carried out to find a best fit model or to constrain the parameters in the flyby. Despite a match in the overall shape, there are a number of discrepancies between the model and the observations. For example, the streamer extends to a larger distance and continuously fades outward in the synthetic NIR image, while the observed streamer bends at its end and ends more sharply. Moreover, the synthetic image shows another spiral arm in the north side of the disk interior to $1''$, which is not seen in observed scattered light (although there are hints of a secondary arm at this distance in the ALMA dust and gas emission maps; Figs. 1 and 2). The observed streamer is also more than one order of magnitude brighter than that in the model. These discrepancies are likely the result of the model having a different orbit of the intruder, a different initial disk size, a different viewing orientation, and/or different scattering properties of the dust from the Z CMa system. In addition, the S/N ratio interior to $1''$ in the Subaru observation may not be high enough to reveal structures.

Keck/NIRC2 archive data. The ALMA source C is located outside the field-of-view (FoV) in Subaru/HiCIAO observations (Fig. 1a). In Fig. 4 we present H -band Keck/NIRC2 observations taken on 2005 Oct 21 (Keck program ID: U14N2), which have a FoV large enough to cover C ($10'' \times 10''$). The Keck data were taken with a coronagraph. The total exposure time is 10 seconds. We conducted the standard calibration procedure: dark subtraction, flat fielding, and hot/bad pixel correction. No point sources are detected at the position of source C. According to the NIRC2 observer’s manual, the zero-point magnitude at the H -band is 25.4 mag. The background noise including photon noise of the central star and the sky noise at the position of the point source C is 23.7 mag, and thus, the 5σ detection limit of the point source C at the H band is 21.9 mag in apparent magnitude.

Circumstellar extinction of component C. Our experiments show that a flyby object with $q \gtrsim 0.1$ is needed to induce the observed streamer, corresponding to $M_C \gtrsim 0.6M_\odot$. A 2 Myr, a $0.6M_\odot$ YSO has a photospheric luminosity of 13.3 mag at 1125 pc in apparent magnitude at H -band²⁶. Thus, an extinction of $A_H > 8$ mag is needed to render component C undetected in the Keck observations. A flyby object on a grazing or penetrating orbit may capture material from the primary disk^{6,24,27,65}. It may also possess circumstellar material prior to the flyby. The estimated dust mass in the circumstellar material around C is $28 \pm 1 M_\oplus$ based on its 1.3 mm flux, which may provide sufficiently large extinction. For example, if

one Lunar mass of interstellar medium dust with $\kappa = 5300 \text{ cm}^2 \text{ g}^{-1}$ at H -band⁶⁶ are distributed spherically symmetrically with a radial density profile $\rho \propto r^{-1.5}$ between 1 to 10 au, the resulting extinction at A_H reaches 10 mag. Alternatively, if C acquires an edge on disk after the flyby, the stellar component can be completely obscured⁶⁷ too. Modeling the specific circumstellar environment around C after the flyby is difficult, due to our ignorance of its state prior to the flyby.

We note that Class 0 YSOs, protostars embedded in a substantial natal envelope, have spectral energy distributions peaking around or longward of $100 \mu\text{m}$ ⁶⁸. Such objects are often detectable only at far-infrared and millimeter wavelengths⁶⁹. However, source C is unlikely to belong to this class. Its gas emission is confined to a region 200 au in size (Fig. 2), inconsistent with the thousands of au size of the envelope of Class 0 objects⁷⁰. In addition, the envelope would likely be distorted and stretched due to the gravitational interaction with the primary, which is not seen. Class 0 objects usually have $M_\star < M_{\text{envelope}}$ ⁷¹. The observed 1.3 mm flux from C corresponds to a total gas+dust mass of $0.01 M_\odot$, assuming a gas-to-dust mass ratio of 100, which is two orders of magnitude smaller than the estimated mass of component C.

Comparisons of the Z CMa system with other flyby candidate systems. A handful of systems with disks undergoing possible stellar flybys have been proposed before, such as RW Aur^{72,73}, AS 205⁷⁴, and UX Tau^{75,76}. However, the unbound nature of the perturber in them does not have strong observational support and remains to be confirmed. For example, latest observations suggest that the two components in RW Aur form a bound binary, as the disk morphology is inconsistent with a one-off encounter⁷⁷. In the bound companion case the circumprimary disk is expected to be severely truncated and the spirals tightly wound and symmetric^{78,79}. The radial extent and the shape of the spiral and the disk in Z CMa strongly favor an unbound perturber. In addition, multiple encounters with a bound companion drive a pair of symmetric arms even if the orbit of the companion is significantly misaligned from the circumprimary disk^{80,81}. This is not seen in Z CMa but seen in other proposed flyby systems. The streamer in Z CMa is convincingly detected in all three tracers (scattered light, and gas and dust emission), which is not the case in other systems. Moreover, the more compact streamer in mm dust continuum than in scattered light, as well as the burster nature of the hosts in Z CMa, support a recent flyby as shown by simulations^{6,24}.

Flyby occurrence rate estimate. In young clusters with a stellar mass density ρ_{cluster} of a few 100s–1000 $M_\odot \text{ pc}^{-3}$, one can estimate the average time required for a particular star to experience a flyby by another star passing within a pericenter distance r_{peri} as^{82,83}:

$$\tau \sim 33 \text{ Myr} \left(\frac{200 M_\odot \text{ pc}^{-3}}{\rho_{\text{cluster}}} \right) \left(\frac{v_\infty}{1 \text{ km s}^{-1}} \right) \left(\frac{1000 \text{ au}}{r_{\text{peri}}} \right) \left(\frac{M_\odot}{M_t} \right) \quad (2)$$

where v_∞ is the mean relative speed of the stars in the cluster at infinity, and M_t is the total mass of the stars involved in the encounter. The last term represents the effect of gravitational focusing, as cross sections are increased as stars are deflected towards each other due to mutual gravitational attraction. Large disks around massive stars are most susceptible to close encounters.

For $r_{\text{peri}} \sim 3000 \text{ au}$, $M_t \sim 10 M_\odot$, $v_\infty \sim 1 \text{ km s}^{-1}$ (typical velocity dispersions in low mass star

forming clusters^{84,85}), and $\rho_{\text{cluster}} \sim 200M_{\odot} \text{ pc}^{-3}$ (typical for nearby star forming clusters⁸⁶), the average encounter time is about 10 Myr, comparable to the age of Z CMA. Other encounter timescale estimates yield similar results^{65,87}. Patchy stellar distribution within dense groups⁸⁸ and mass segregation leading to massive stars, such as Z CMA, being located in the central region with the highest density could further shrink the encounter timescale. Although the stellar mass density in the environment of Z CMA is not known accurately, we note that the binary is located close to the center of a star-forming molecular gas filament over $3'$ ($\sim 1 \text{ pc}$) in length⁸⁹, and a relatively high ρ_{cluster} is expected. Overall, it is reasonable to expect the Z CMA system to have experienced disk-perturbing flyby events at its young age. Simulations have also shown that^{2,83,90,91} such encounters are common in the center of young dense clusters, and outburst-inducing encounters are more likely for massive stars.

Data availability Raw ALMA data is publicly available via the ALMA archive <https://almascience.eso.org/aq/> under project IDs 2016.1.00110.S and 2016.2.00168.S. Raw JVLA data is publicly available via the JVLA archive <https://archive.nrao.edu/archive/advquery.jsp> under project code 16B-080. Raw Keck data is publicly available via the KOA Data Access Service <http://koa.ipac.caltech.edu/> under the program ID U14N2. Final reduced and calibrated image files are available at <https://doi.org/10.6084/m9.figshare.16915327>.

Code availability The PHANTOM code is made available at <https://github.com/danieljprice/phantom> by Daniel Price. The MCFOST code is made available at <https://github.com/cpinte/mcfost> by Christophe Pinte.

Supplementary Information is available in the online version of the paper.

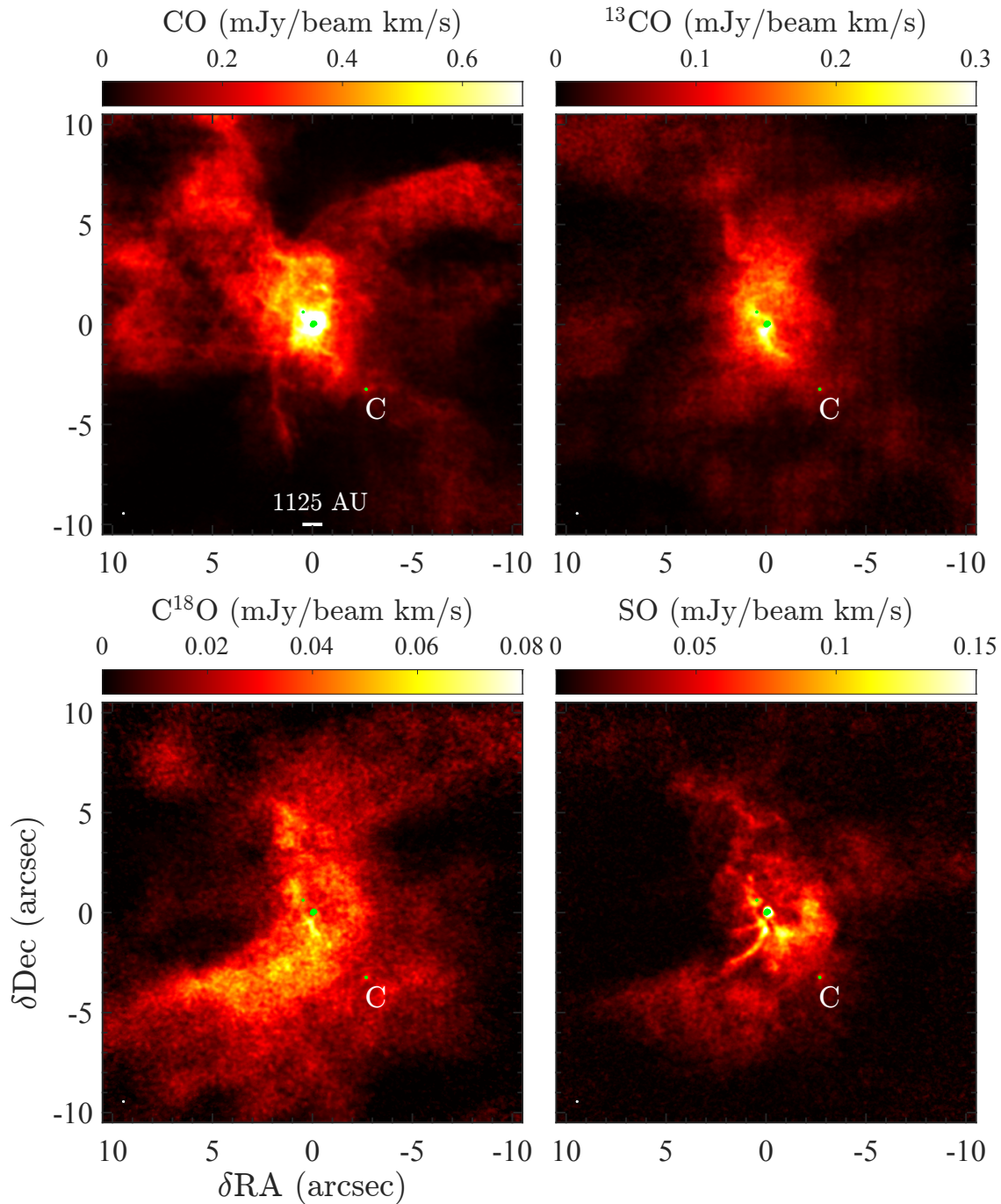
Acknowledgements We thank Chul-Hwan Kim, Jeongeun Lee, and Hongping Deng for helpful discussions. R.D. would like to thank Luyi Xu for the support and encouragement in the period of this work. R.D. acknowledges financial support provided by the Natural Sciences and Engineering Research Council of Canada through a Discovery Grant, as well as the Alfred P. Sloan Foundation through a Sloan Research Fellowship. N.C. acknowledges support from the European Union’s Horizon 2020 research and innovation programme under the Marie Skłodowska-Curie grant agreement No 210021. H.B.L. acknowledges support from the Ministry of Science and Technology (MoST) of Taiwan (grant No. 108-2112-M-001-002-MY3). E.I.V. acknowledges support from the Russian Fund for Fundamental Research, Russian-Taiwanese project 19-52-52011. Y.H. is supported by the Jet Propulsion Laboratory, California Institute of Technology, under a contract with the National Aeronautics and Space Administration. A.K. and L.C. acknowledge support from the European Research Council (ERC) under the European Union’s Horizon 2020 research and innovation programme under grant agreement No 716155 (SACCRED). L.C. is supported by the Hungarian OTKA grant K132406. M.T. is supported by the Ministry of Science and Technology (MoST) of Taiwan (grant No. 106-2119-M-001-026-MY3, 109-2112-M-001-019). H.B.L. and M.T. and are supported by MoST of Taiwan 108-2923-M-001-006-MY3 for the Taiwanese-Russian collaboration project. The Geryon cluster at the Centro de Astro-Ingenieria UC was extensively used for the calculations performed in this paper. BASAL CATA PFB-06, the Anillo ACT-86, FONDEQUIP AIC-57, and QUIMAL 130008 provided funding for several improvements to the Geryon cluster. This paper makes use of the following ALMA data: ADS/JAO.ALMA#2016.1.00110.S and #2016.2.00168.S. ALMA is a partnership of ESO (representing its member states), NSF (USA) and NINS (Japan), together with NRC (Canada), MOST and ASIAA (Taiwan), and KASI (Republic of Korea), in cooperation with the Republic of Chile. The Joint ALMA Observatory is operated by ESO, au/NRAO and NAOJ. The National Radio Astronomy Observatory is a facility of the National Science Foundation operated under cooperative agreement by Associated Universities, Inc.

Author Contributions R.D. led the ALMA proposals. H.L. led the JVLA proposal and processed the ALMA and JVLA data. N.C. and C.P. performed the hydrodynamics and radiative transfer simulations. R.D., H.L., N.C., and C.P. wrote the manuscript. All co-authors provided input to the observational proposals and/or the manuscript.

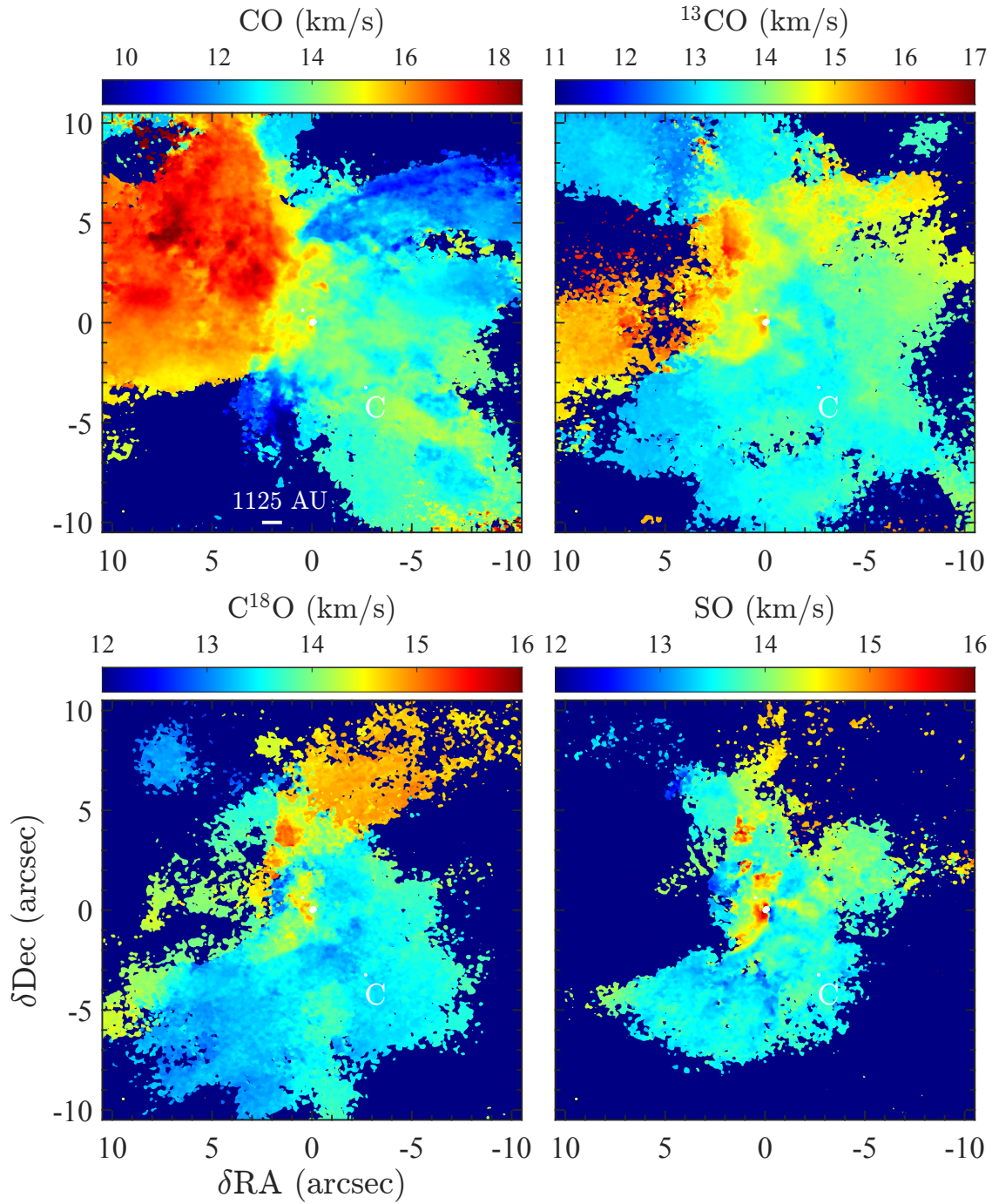
Competing Interests The authors declare that they have no competing financial interests.

Correspondence Correspondence and requests for materials should be addressed to R.D. (email: rbdong@uvic.ca), H.L. (email: hyliau@asiaa.sinica.edu.tw), N.C. (nicolas.cuello@univ-grenoble-alpes.fr), and C.P. (christophe.pinte@monash.edu).

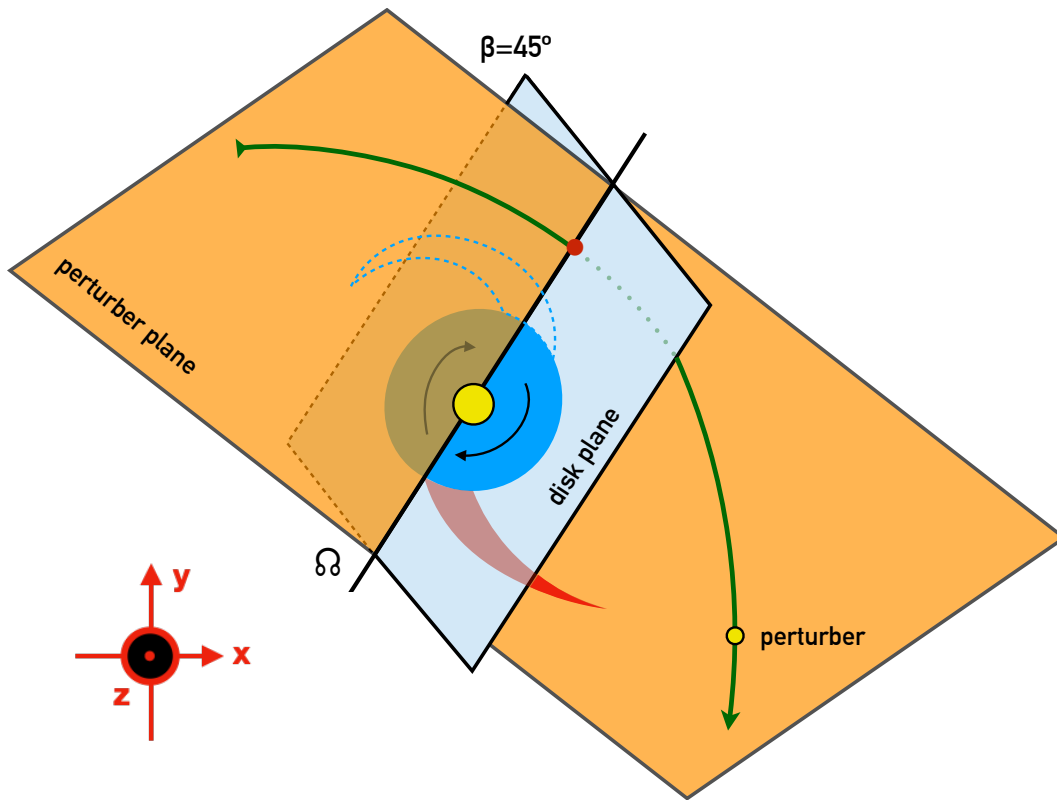
Extended Data (Figures and tables in the Methods Section)



Extended data figure 1: Integrated intensity (moment 0) maps of the ^{12}CO (2-1), ^{13}CO (2-1), C^{18}O (2-1), and $\text{SO } ^3\Sigma 6(5)\text{-}5(4)$ transitions on a large scale. The beam size ($0.19'' \times 0.18''$; P.A.= 88°) is marked at the lower left corner. The Robust = 0 weighted 224 GHz continuum image (beam size $0''.075 \times 0''.047$; P.A.= 65°) is shown in green contours at 0.13 and 1.3 mJy beam $^{-1}$ levels (5 and 50 \times the root mean square noises) to highlight the four compact continuum sources. The ALMA/VLA source C is labeled.



Extended data figure 2: Moment-1 maps (intensity-weighted mean velocity) of the gas observations. The Robust = 0 weighted 224 GHz continuum image (beam size $0''.075 \times 0''.047$; P.A.= 65°) is shown in white contours at 0.13 and 1.3 mJy beam $^{-1}$ levels (5 and 50 \times the root mean square noises). The systematic velocity is ~ 14 km/s⁹². The ALMA/VLA source C is labeled.



Extended data figure 3: Sketch of the flyby simulation geometry. The perturber's orbital plane is in orange. The plane of the initial circumprimary disk is in blue. The primary spiral pointing towards the perturber is in solid red and is in the plane of the perturber. The secondary spiral is in dashed red and in the plane of the circumprimary disk. The line of sight is in the z direction.

Extended data table 1: Gaussian fitting of point-like components detected around ZCMa^a

#	R.A. (J2000)	Decl. (J2000)	Peak intensity ($\mu\text{Jy beam}^{-1}$)	Gaussian fitted flux (μJy)	a^b (mas)	b^c (mas)	P.A. ^d (degree)
ALMA 224.247 GHz, Briggs Robust = 0 weighted ($\theta_{\text{maj}} \times \theta_{\text{min}}=0''.078 \times 0''.046$; P.A.=66°)							
A	07 ^h 03 ^m 43 ^s .154	-11°33'06''.13	21000±410	24000±810	23±6.8	22±9.1	82±86
B	07 ^h 03 ^m 43 ^s .159	-11°33'06''.22	4100±62	4700±120	26±5.8	20±5.9	71±61
C	07 ^h 03 ^m 42 ^s .976	-11°33'09''.43	480±26	700±40	43±8.5	35±7.6	51±84
D	07 ^h 03 ^m 43 ^s .191	-11°33'05''.56	560±26	550±24	... ^f
JVLA 32.998 GHz, Briggs Robust = 0 weighted ($\theta_{\text{maj}} \times \theta_{\text{min}}=0''.070 \times 0''.049$; P.A.=2.5°)							
A	07 ^h 03 ^m 43 ^s .153	-11°33'06''.14	630±28	780±57	37±7.7	18±13	80±49
B	07 ^h 03 ^m 43 ^s .158	-11°33'06''.22	260±11	390±29	59±9.8	33±12	38±23
C	07 ^h 03 ^m 42 ^s .975	-11°33'09''.46	24±5.2 ^e	27±5.2

^a Gaussian fittings may be confused by extended dust emission. While we treat the Gaussian fitted flux as the total flux and use it in dust mass estimates, the true total flux from each source may be in between the peak intensity and the Gaussian fitted flux.

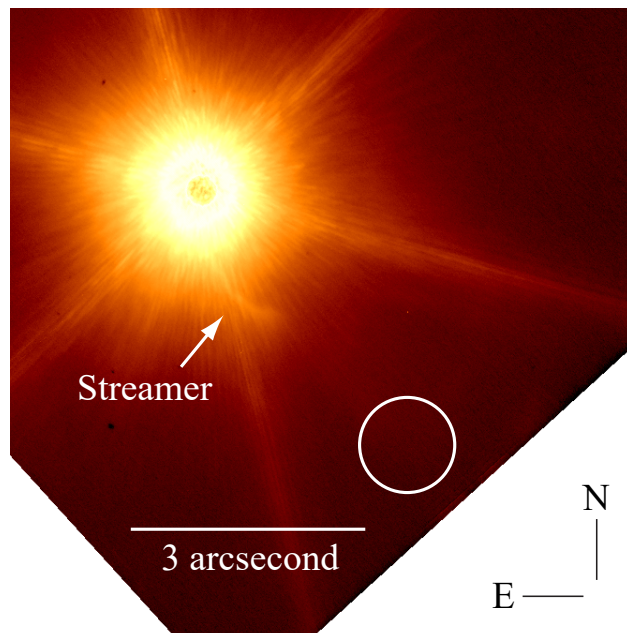
^b Gaussian deconvolved major axis FWHM.

^c Gaussian deconvolved minor axis FWHM.

^d Gaussian deconvolved position angle.

^e Only detected from the Robust = 2 weighted image, with $\theta_{\text{maj}} \times \theta_{\text{min}}=100 \times 66$ mas (P.A.=19°).

^f Gaussian fitting results indicate that the source is consistent with a δ function with non-detectable size.).



Extended data figure 4: Keck/NIRC2 *H*-band archive data of Z CMa. The data were taken in 2005 Oct 21. White circle indicates the position of the point source C.

1. Offner, S. S. R., Klein, R. I. & McKee, C. F. Driven and Decaying Turbulence Simulations of Low-Mass Star Formation: From Clumps to Cores to Protostars. *Astrophys. J.* **686**, 1174–1194 (2008).
2. Bate, M. R. Stellar, brown dwarf and multiple star properties from a radiation hydrodynamical simulation of star cluster formation. *Mon. Not. R. Astron. Soc.* **419**, 3115–3146 (2012).
3. Kuruwita, R. L., Federrath, C. & Haugbølle, T. The dependence of episodic accretion on eccentricity during the formation of binary stars. *Astron. Astrophys.* **641**, A59 (2020).
4. Audard, M. *et al.* Episodic Accretion in Young Stars. *Protostars and Planets VI* 387–410 (2014).
5. Pfalzner, S., Tackenberg, J. & Steinhausen, M. Accretion bursts in young stars driven by the cluster environment. *Astron. Astrophys.* **487**, L45–L48 (2008).
6. Cuello, N. *et al.* Flybys in protoplanetary discs: I. Gas and dust dynamics. *Mon. Not. R. Astron. Soc.* **483**, 4114–4139 (2019).
7. Dullemond, C. P. *et al.* Cloudlet capture by transitional disk and FU Orionis stars. *Astron. Astrophys.* **628**, A20 (2019).
8. Vorobyov, E. I., Elbakyan, V. G., Liu, H. B. & Takami, M. Distinguishing between different mechanisms of FU-Orionis-type luminosity outbursts. *Astron. Astrophys.* **647**, A44 (2021).
9. Hartmann, L. *et al.* Pre–Main-Sequence Disk Accretion in Z Canis Majoris. *Astrophys. J.* **338**, 1001–1010 (1989).
10. Bonnefoy, M. *et al.* The 2008 outburst in the young stellar system Z CMa. III. Multi-epoch high-angular resolution images and spectra of the components in near-infrared. *Astron. Astrophys.* **597**, A91 (2017).
11. Hinkley, S. *et al.* High-resolution Infrared Imaging and Spectroscopy of the Z Canis Majoris System during Quiescence and Outburst. *Astrophys. J.* **763**, L9 (2013).
12. Millan-Gabet, R. & Monnier, J. D. Discovery of a Near-Infrared Jetlike Feature in the Z Canis Majoris System. *Astrophys. J.* **580**, L167–L170 (2002).
13. Canovas, H. *et al.* The inner environment of Z Canis Majoris: High-contrast imaging polarimetry with NaCo. *Astron. Astrophys.* **578**, L1 (2015).
14. Alonso-Albi, T. *et al.* Circumstellar disks around Herbig Be stars. *Astron. Astrophys.* **497**, 117–136 (2009).
15. Liu, H. B. *et al.* Absence of Significant Cool Disks in Young Stellar Objects Exhibiting Repetitive Optical Outbursts. *Astrophys. J. Lett.* **816**, L29 (2016).
16. Liu, H. B. *et al.* A concordant scenario to explain FU Orionis from deep centimeter and millimeter interferometric observations. *Astron. Astrophys.* **602**, A19 (2017).
17. Li, J. I., Liu, H. B., Hasegawa, Y. & Hirano, N. Systematic Analysis of Spectral Energy Distributions and the Dust Opacity Indices for Class 0 Young Stellar Objects. *Astrophys. J.* **840**, 72 (2017).

18. Liu, H. B. The Anomalously Low (Sub)Millimeter Spectral Indices of Some Protoplanetary Disks May Be Explained By Dust Self-scattering. *Astrophys. J. Lett.* **877**, L22 (2019).
19. Kuffmeier, M., Calcutt, H. & Kristensen, L. E. The bridge: a transient phenomenon of forming stellar multiples. Sequential formation of stellar companions in filaments around young protostars. *Astron. Astrophys.* **628**, A112 (2019).
20. Lee, A. T., Offner, S. S. R., Kratter, K. M., Smullen, R. A. & Li, P. S. The Formation and Evolution of Wide-orbit Stellar Multiples In Magnetized Clouds. *Astrophys. J.* **887**, 232 (2019).
21. Liu, H. B. *et al.* Circumstellar disks of the most vigorously accreting young stars. *Science Advances* **2**, e1500875 (2016).
22. Dong, R., Vorobyov, E., Pavlyuchenkov, Y., Chiang, E. & Liu, H. B. Signatures of Gravitational Instability in Resolved Images of Protostellar Disks. *Astrophys. J.* **823**, 141 (2016).
23. Pfalzner, S. Spiral Arms in Accretion Disk Encounters. *Astrophys. J.* **592**, 986–1001 (2003).
24. Cuello, N. *et al.* Flybys in protoplanetary discs - II. Observational signatures. *Mon. Not. R. Astron. Soc.* **491**, 504–514 (2020).
25. Vorobyov, E. I. & Elbakyan, V. G. Gravitoviscous protoplanetary disks with a dust component. II. Spatial distribution and growth of dust in a clumpy disk. *Astron. Astrophys.* **631**, A1 (2019).
26. Baraffe, I., Homeier, D., Allard, F. & Chabrier, G. New evolutionary models for pre-main sequence and main sequence low-mass stars down to the hydrogen-burning limit. *Astron. Astrophys.* **577**, A42 (2015).
27. Vorobyov, E. I. *et al.* The origin of tail-like structures around protoplanetary disks. *Astron. Astrophys.* **635**, A196 (2020).
28. Vorobyov, E. I., Steinrueck, M. E., Elbakyan, V. & Guedel, M. Formation of freely floating sub-stellar objects via close encounters. *Astron. Astrophys.* **608**, A107 (2017).
29. Winter, A. J., Clarke, C. J., Rosotti, G. & Booth, R. A. Protoplanetary disc response to distant tidal encounters in stellar clusters. *Mon. Not. R. Astron. Soc.* **475**, 2314–2325 (2018).
30. Kuffmeier, M., Dullemond, C. P., Reissl, S. & Goicovic, F. G. Misaligned disks induced by infall. *arXiv e-prints* arXiv:2110.04309 (2021).
31. Dunham, M. M. & Vorobyov, E. I. Resolving the Luminosity Problem in Low-mass Star Formation. *Astrophys. J.* **747**, 52 (2012).
32. Meyer, D. M. A. *et al.* Burst occurrence in young massive stellar objects. *Monthly Notices of the Royal Astronomical Society* **482**, 5459–5476 (2019).
33. Vorobyov, E. I. Ejection of gaseous clumps from gravitationally unstable protostellar disks. *Astron. Astrophys.* **590**, A115 (2016).

34. Kratter, K. M., Murray-Clay, R. A. & Youdin, A. N. The Runts of the Litter: Why Planets Formed Through Gravitational Instability Can Only Be Failed Binary Stars. *Astrophys. J.* **710**, 1375–1386 (2010).
35. Basu, S. & Vorobyov, E. I. A Hybrid Scenario for the Formation of Brown Dwarfs and Very Low Mass Stars. *Astrophys. J.* **750**, 30 (2012).
36. Grady, C. A. *et al.* Hubble Space Telescope Space Telescope Imaging Spectrograph Coronagraphic Imaging of the Herbig AE Star AB Aurigae. *Astrophys. J. Lett.* **523**, L151–L154 (1999).
37. Fukagawa, M. *et al.* Spiral Structure in the Circumstellar Disk around AB Aurigae. *Astrophys. J. Lett.* **605**, L53–L56 (2004).
38. Pineda, J. E. *et al.* A protostellar system fed by a streamer of 10,500 au length. *Nature Astronomy* **4**, 1158–1163 (2020).
39. Ginski, C. *et al.* Disk Evolution Study Through Imaging of Nearby Young Stars (DESTINYs): Late Infall Causing Disk Misalignment and Dynamic Structures in SU Aur. *Astrophys. J. Lett.* **908**, L25 (2021).
40. Huang, J. *et al.* Molecules with ALMA at Planet-forming Scales (MAPS) XIX. Spiral Arms, a Tail, and Diffuse Structures Traced by CO around the GM Aur Disk. *arXiv e-prints* arXiv:2109.06224 (2021).
41. Brown, M. E., Trujillo, C. & Rabinowitz, D. Discovery of a Candidate Inner Oort Cloud Planetoid. *Astrophys. J.* **617**, 645–649 (2004).
42. Schwamb, M. E., Brown, M. E., Rabinowitz, D. L. & Ragozzine, D. Properties of the Distant Kuiper Belt: Results from the Palomar Distant Solar System Survey. *Astrophys. J.* **720**, 1691–1707 (2010).
43. Duchêne, G. & Kraus, A. Stellar Multiplicity. *Annu. Rev. Astron. Astrophys.* **51**, 269–310 (2013).
44. Lindegren, L. *et al.* Gaia Early Data Release 3. The astrometric solution. *Astron. Astrophys.* **649**, A2 (2021).
45. Clariá, J. J. A study of the stellar association Canis Major OB 1. *Astron. Astrophys.* **37**, 229–236 (1974).
46. Kaltcheva, N. T. & Hilditch, R. W. The distribution of bright OB stars in the Canis Major-Puppis-Vela region of the Milky Way. *Mon. Not. R. Astron. Soc.* **312**, 753–768 (2000).
47. Takami, M. *et al.* Near-infrared High-resolution Imaging Polarimetry of FU Ori-type Objects: Toward a Unified Scheme for Low-mass Protostellar Evolution. *Astrophys. J.* **864**, 20 (2018).
48. Herbig, G. H. & Bell, K. R. *Third Catalog of Emission-Line Stars of the Orion Population : 3 : 1988* (Lick Observatory, 1988).
49. Ikeda, H. *et al.* Sequential Star Formation in a Cometary Globule (BRC37) of IC1396. *Astron. J.* **135**, 2323–2335 (2008).

50. Fernandes, B., Gregorio-Hetem, J., Montmerle, T. & Rojas, G. Spectroscopic characterization of X-ray emitting young stars associated with the Sh 2-296 nebula. *Mon. Not. R. Astron. Soc.* **448**, 119–134 (2015).
51. Ducourant, C. *et al.* Pre-main sequence star Proper Motion Catalogue. *Astron. Astrophys.* **438**, 769–778 (2005).
52. McMullin, J. P., Waters, B., Schiebel, D., Young, W. & Golap, K. CASA Architecture and Applications. In Shaw, R. A., Hill, F. & Bell, D. J. (eds.) *Astronomical Data Analysis Software and Systems XVI*, vol. 376 of *Astronomical Society of the Pacific Conference Series*, 127 (2007).
53. Sault, R. J., Teuben, P. J. & Wright, M. C. H. A Retrospective View of MIRIAD. In Shaw, R. A., Payne, H. E. & Hayes, J. J. E. (eds.) *Astronomical Data Analysis Software and Systems IV*, vol. 77 of *Astronomical Society of the Pacific Conference Series*, 433 (1995).
54. Beckwith, S. V. W., Sargent, A. I., Chini, R. S. & Guesten, R. A survey for circumstellar disks around young stellar objects. *Astron. J.* **99**, 924–945 (1990).
55. Price, D. J. *et al.* Phantom: A Smoothed Particle Hydrodynamics and Magnetohydrodynamics Code for Astrophysics. *Publ. Astron. Soc. Aust.* **35**, e031 (2018).
56. Lodato, G. & Price, D. J. On the diffusive propagation of warps in thin accretion discs. *Mon. Not. R. Astron. Soc.* **405**, 1212–1226 (2010).
57. Dong, R., Fung, J. & Chiang, E. How Spirals and Gaps Driven by Companions in Protoplanetary Disks Appear in Scattered Light at Arbitrary Viewing Angles. *Astrophys. J.* **826**, 75 (2016).
58. Bate, M. R., Bonnell, I. A. & Price, N. M. Modelling accretion in protobinary systems. *Mon. Not. R. Astron. Soc.* **277**, 362–376 (1995).
59. Pinte, C., Ménard, F., Duchêne, G. & Bastien, P. Monte Carlo radiative transfer in protoplanetary disks. *Astron. Astrophys.* **459**, 797–804 (2006).
60. Pinte, C. *et al.* Benchmark problems for continuum radiative transfer. High optical depths, anisotropic scattering, and polarisation. *Astron. Astrophys.* **498**, 967–980 (2009).
61. Siess, L., Dufour, E. & Forestini, M. An internet server for pre-main sequence tracks of low- and intermediate-mass stars. *Astron. Astrophys.* **358**, 593–599 (2000).
62. Allard, F., Homeier, D. & Freytag, B. Models of very-low-mass stars, brown dwarfs and exoplanets. *Philosophical Transactions of the Royal Society of London Series A* **370**, 2765–2777 (2012).
63. Vorobyov, E. I. & Elbakyan, V. G. Gravitational fragmentation and formation of giant protoplanets on orbits of tens of au. *Astron. Astrophys.* **618**, A7 (2018).
64. Weingartner, J. C. & Draine, B. T. Dust Grain-Size Distributions and Extinction in the Milky Way, Large Magellanic Cloud, and Small Magellanic Cloud. *Astrophys. J.* **548**, 296–309 (2001).

65. Forgan, D. & Rice, K. Stellar encounters in the context of outburst phenomena. *Mon. Not. R. Astron. Soc.* **402**, 1349–1356 (2010).
66. Takami, M. *et al.* High-contrast Near-infrared Imaging Polarimetry of the Protoplanetary Disk around RY TAU. *Astrophys. J.* **772**, 145 (2013).
67. Terada, H. *et al.* Detection of Water Ice in Edge-on Protoplanetary Disks: HK Tauri B and HV Tauri C. *Astrophys. J.* **667**, 303–307 (2007).
68. Frost, A. J., Oudmaijer, R. D., de Wit, W. J. & Lumsden, S. L. A multi-scale exploration of a massive young stellar object. A transition disk around G305.20+0.21? *Astron. Astrophys.* **625**, A44 (2019).
69. Gerin, M. *et al.* Evidence for disks at an early stage in class 0 protostars? *Astron. Astrophys.* **606**, A35 (2017).
70. Gaudel, M. *et al.* Angular momentum profiles of Class 0 protostellar envelopes. *Astron. Astrophys.* **637**, A92 (2020).
71. Flores-Rivera, L. *et al.* Physical and Chemical Structure of the Disk and Envelope of the Class 0/I Protostar L1527. *Astrophys. J.* **908**, 108 (2021).
72. Cabrit, S., Pety, J., Pesenti, N. & Dougados, C. Tidal stripping and disk kinematics in the RW Aurigae system. *Astron. Astrophys.* **452**, 897–906 (2006).
73. Dai, F., Facchini, S., Clarke, C. J. & Haworth, T. J. A tidal encounter caught in the act: modelling a star-disc fly-by in the young RW Aurigae system. *Mon. Not. R. Astron. Soc.* **449**, 1996–2009 (2015).
74. Kurtovic, N. T. *et al.* The Disk Substructures at High Angular Resolution Project (DSHARP). IV. Characterizing Substructures and Interactions in Disks around Multiple Star Systems. *Astrophys. J.* **869**, L44 (2018).
75. Ménard, F. *et al.* Ongoing flyby in the young multiple system UX Tauri. *Astron. Astrophys.* **639**, L1 (2020).
76. Zapata, L. A. *et al.* Tidal Interaction between the UX Tauri A/C Disk System Revealed by ALMA. *Astrophys. J.* **896**, 132 (2020).
77. Rodriguez, J. E. *et al.* Multiple Stellar Flybys Sculpting the Circumstellar Architecture in RW Aurigae. *Astrophys. J.* **859**, 150 (2018).
78. Dong, R. *et al.* An M Dwarf Companion and Its Induced Spiral Arms in the HD 100453 Protoplanetary Disk. *Astrophys. J. Lett.* **816**, L12 (2016).
79. Wagner, K. *et al.* The Orbit of the Companion to HD 100453A: Binary-driven Spiral Arms in a Protoplanetary Disk. *Astrophys. J.* **854**, 130 (2018).
80. van der Plas, G. *et al.* ALMA study of the HD 100453 AB system and the tidal interaction of the companion with the disk. *Astron. Astrophys.* **624**, A33 (2019).

81. Rosotti, G. P. *et al.* Spiral arms in the protoplanetary disc HD100453 detected with ALMA: evidence for binary-disc interaction and a vertical temperature gradient. *Mon. Not. R. Astron. Soc.* **491**, 1335–1347 (2020).
82. Davies, M. B. Turning solar systems into extrasolar planetary systems in stellar clusters. In Sozzetti, A., Lattanzi, M. G. & Boss, A. P. (eds.) *The Astrophysics of Planetary Systems: Formation, Structure, and Dynamical Evolution*, vol. 276 of *IAU Symposium*, 304–307 (2011).
83. Pfalzner, S. Early evolution of the birth cluster of the solar system. *Astron. Astrophys.* **549**, A82 (2013).
84. Cottaar, M. *et al.* IN-SYNC. III. The Dynamical State of IC 348 - A Super-virial Velocity Dispersion and a Puzzling Sign of Convergence. *Astrophys. J.* **807**, 27 (2015).
85. Foster, J. B. *et al.* IN-SYNC. II. Virial Stars from Subvirial Cores—the Velocity Dispersion of Embedded Pre-main-sequence Stars in NGC 1333. *Astrophys. J.* **799**, 136 (2015).
86. Lada, C. J. & Lada, E. A. Embedded Clusters in Molecular Clouds. *Annu. Rev. Astron. Astrophys.* **41**, 57–115 (2003).
87. Clarke, C. J. & Pringle, J. E. Star-disc interactions and binary star formation. *Mon. Not. R. Astron. Soc.* **249**, 584–587 (1991).
88. Joncour, I., Duchêne, G., Moraux, E. & Motte, F. Multiplicity and clustering in Taurus star forming region. II. From ultra-wide pairs to dense NESTs. *Astron. Astrophys.* **620**, A27 (2018).
89. Sandell, G. & Weintraub, D. A. On the Similarity of FU Orionis Stars to Class I Protostars: Evidence from the Submillimeter. *Astrophys. J. Suppl. Ser.* **134**, 115–132 (2001).
90. Pfalzner, S. Encounter-driven accretion in young stellar clusters - A connection to FUors? *Astron. Astrophys.* **492**, 735–741 (2008).
91. Bate, M. R. On the diversity and statistical properties of protostellar discs. *Mon. Not. R. Astron. Soc.* **475**, 5618–5658 (2018).
92. Liljeström, T. & Olofsson, G. Evidence for Infall toward Z Canis Majoris from Radio and Near-Infrared Spectroscopy. *Astrophys. J.* **478**, 381–394 (1997).